Published in final edited form as:

Nat Photonics. 2016 August ; 10(8): 534–540. doi:10.1038/nphoton.2016.94.

Stain-free histopathology by programmable supercontinuum pulses

Haohua Tu[1,*,†], **Yuan Liu**[1,†], **Dmitry Turchinovich**[2], **Marina Marjanovic**[1,2], **Jens Lyngsø**[3], **Jesper Lægsgaard**[4], **Eric J. Chaney**[1], **Youbo Zhao**[1], **Sixian You**[1,2], **William L. Wilson**[5], **Bingwei Xu**[6], **Marcos Dantus**[7], and **Stephen A. Boppart**[1,2,8,9,*]

[1]Beckman Institute for Advanced Science and Technology, University of Illinois at Urbana-Champaign, Urbana, IL 61801, USA

[2]Department of Bioengineering, University of Illinois at Urbana-Champaign, Urbana, IL 61801, USA, [2]Max Planck Institute for Polymer Research, Ackermannweg 10, Mainz, 55128, Germany

[3]NKT Photonics A/S, Blokken 84, 3460 Birkerød, Denmark

[4]DTU Fotonik, Technical University of Denmark, Ørsteds Plads 343, 2800 Lyngby, Denmark

[5]Department of Materials Science and Engineering, Frederick Seitz Materials Research Laboratory, University of Illinois at Urbana-Champaign, Urbana, Illinois 61801, USA

[6]Biophotonic Solutions Inc., East Lansing, Michigan 48823, USA

[7]Department of Chemistry and Department of Physics, Michigan State University, East Lansing, Michigan 48824, USA

[8]Department of Electrical and Computer Engineering, University of Illinois at Urbana-Champaign, Urbana, IL 61801, USA

[9]College of Medicine, University of Illinois at Urbana-Champaign, Urbana, IL 61801, USA

Abstract

The preparation, staining, visualization, and interpretation of histological images of tissue is well-accepted as the gold standard process for the diagnosis of disease. These methods were developed historically, and are used ubiquitously in pathology, despite being highly time and labor intensive. Here we introduce a unique optical imaging platform and methodology for label-free multimodal

[*]Correspondence and requests for materials should be addressed to H. T. and S. A. B., boppart@illinois.edu, htu@illinois.edu.
[†]These authors contributed equally to this work.

Author Contributions

Tu, H., Liu, Y., and Boppart, S. A. conceived the idea, performed the analysis, and wrote the manuscript. Tu, H, Liu, Y., and Zhao, Y. built the microscope and conducted optical experiments. Tu, H., Turchinovich, D., and Lægsgaard, J. tested and improved the long-term stability of the fiber supercontinuum source, Lyngsø, J. fabricated a variety of photonic crystal fibers for the supercontinuum source, and Wilson, W. L. characterized the supercontinuum source. Chaney, E. J., You, S., and Marjanovic, M. performed biological experiments. Xu, B. and Dantus, M. built the pulse shaper. Tu, H. and Boppart, S. A. obtained funding for this research.

Supplementary Information is linked to the online version of the paper.

Competing financial interests

The authors declare no competing financial interests.

multiphoton microscopy that uses a novel photonic crystal fiber source to generate tailored chemical contrast based on programmable supercontinuum pulses. We demonstrate collection of optical signatures of the tumor microenvironment, including evidence of mesoscopic biological organization, tumor cell migration, and (lymph-)angiogenesis collected directly from fresh *ex vivo* mammary tissue. Acquisition of these optical signatures and other cellular or extracellular features, which are largely absent from histologically processed and stained tissue, combined with an adaptable platform for optical alignment-free programmable-contrast imaging, offers the potential to translate stain-free molecular histopathology into routine clinical use.

Histopathology, whether visualizing microstructure in standard hematoxylin and eosin (H&E) stained tissue sections or selectively labeling molecules with special immunohistochemical stains, has a long history of development and has been instrumental in biological and clinical laboratories for basic research as well as in hospital pathology labs for disease diagnosis (Supplementary Discussion 1). However, current histopathology techniques have several limitations. First, the histological-histochemical treatment of the tissue, including fixation, embedding, sectioning, and staining, are well known to induce distortion artifacts and loss of some biological components, which dictate the subjectivity of subsequent image-based histopathological observations and interpretations. Second, typical histological processing such as formalin-fixed, paraffin-embedded, H&E-stained histology, requires a significant amount of time, from ~10 hours to a few days (less in the case of the frozen-section analysis specifically used in cancer surgery), and thus delays diagnosis, heightens patient stress, and presents a significant economic burden to society[1]. Third, cost ineffectiveness has been intrinsically associated with the more than 4500 labor-intensive histological-histochemical processes and procedures developed between 1841 and 1950 predominantly (95%)[2].

Due to the time and labor required to process, prepare, stain, and microscopically visualize the tissue, as well as the inherent destructive nature of standard histopathology, great efforts have been made to use multiphoton microscopy[3] for the molecular and cellular examination of unlabeled (fresh) pathological tissue or other biological specimens (Supplementary Table S1). Stain-free histopathology of fresh tissue within minutes has been established by diverse nonlinear optical processes[4–8] to improve upon the conventional histotechnology that is based on single-photon microscopy, so that the time-consuming paradigmatic elements of standard histology procedures may be avoided. However, the ultrafast lasers of multiphoton microscopy have been difficult to use by pathologists with no laser training. In this study, we introduce a user-friendly optical source and platform capable of generating histochemically-specific images without laser realignments normally required for multiphoton microscopy, and provide visualization of microstructures not routinely possible with current histological techniques. In contrast to many earlier studies that only demonstrated the diagnostic capability of multiphoton microscopy to approach that of H&E histology, we show that this versatile multimodal multiphoton microscopy platform based on a widely-coherent supercontinuum source can visualize biological organization of mesoscopic (micron-scale) constituents, discriminate cell types in connective tissue, quantify cellular metabolism, and recognize well-known cancer indictors such as collective tumor cell invasion, tumor-

associated collagen reorganization, angiogenesis, and lymphangiogenesis *in situ* in freshly excised unstained (thick) tissues.

Our technology was first used for observation of the spatial distribution of biological vesicles and elastin fibers in these fresh tissues. To accomplish this, we developed a multiphoton microscope (Supplementary Fig. S1) which employs a novel photonic crystal fiber source and programmed electronic variables (rather than discrete optical alignment settings) to collect co-localized label-free images based on the endogenous contrast from two-photon auto-fluorescence (2PAF), three-photon auto-fluorescence (3PAF), second harmonic generation (SHG), third harmonic generation (THG), and coherent anti-Stokes Raman scattering (CARS) or stimulated Raman scattering (SRS) (Supplementary Tables S1, S2)[9]. A well-known preclinical carcinogen-induced rat mammary tumor model[10] was used, and a mammary tumor/tissue specimen (5×5 mm^2 area with ~1 mm thickness) was excised from a rat six weeks after carcinogen injection. The collection of the multimodal multiphoton images began within minutes after dissection from a site with cleanly delineated adipose and stromal regions, and standard H&E histology was subsequently performed to locate an anatomically similar site for comparison[6] (Fig. 1, left panel). The multiphoton images of R2850 vs. R3050 (CARS response at 2850 cm^{-1} versus 3050 cm^{-1}), THG vs. SHG, and 3PAF vs. 2PAF demonstrate the largely orthogonal signal contrast of lipids vs. proteins-water[6,11], optical heterogeneity vs. noncentrosymmetry, and blue auto-fluorescence vs. yellow FAD auto-fluorescence[12], respectively. These multiple contrast mechanisms highlight the diverse histochemical and structural components of the specimen, particularly the 3PAF-visible micron-sized biological vesicles that appear spatially arranged in a tubular formation. The same field-of-view also displays some uniquely 2PAF-visible thin (~1 μm diameter) elastin fibers (EF) known to be present in mammary stroma (Supplementary Fig. S2). In a second specimen from the same animal, elastin fibers are shown to have organize into a “basket” in adipocyte-infiltrated stroma (Fig. 1, right panel).

The visualization of these structures is somewhat analogous to the visualization of hand bones in 1895 by X-ray radiography. Under ambient visible illumination, the bones are not visible due to low detection sensitivity and high interfering background, even though the information is present. They emerge when the visible illumination is switched to the X-ray irradiation at a different wavelength. Thus, imaging contrast from a fresh unstained tissue specimen can be generated by simply manipulating an irradiative wave that interacts with the specimen, rather than by manipulating (e.g., histologically processing and staining) the specimen and irradiating it with a fixed wave. This methodology of clinical imaging[13] has been largely inherited in various radiological modalities (ultrasound, CT, MRI, PET, etc.) and in multiphoton imaging that enables stain-free histopathology[4–8], allowing the imaging to rely more on physics (wave propagation, electrical engineering, programming, etc.) than chemistry (wet laboratories, reagents, consumables, etc.). Noticeably, the above visualization of these biological structures marks a shift from subcellular chemical contrast generation based on histological and histochemical sample treatments to one of light manipulations by programmable multiphoton irradiation and signal detection. The only settings varied between the single-modality images in Fig. 1 are to control an electronic amplitude-phase mask of the pulse shaper for tailored excitation to pair with a switchable spectral channel for signal detection (Supplementary Table S2), and an electronic setting of

optical delay that sets the CARS vibrational frequency. Since these settings can be rapidly tuned (<10 ms) or switched under programmable control, different histochemical components can be selectively revealed in different single-modality images, highlighting our perception of "seeing things in a different light". By varying the light with agile pseudo-continuous programming, the contrast of these components against their background can be rapidly tuned to discover the otherwise obscured biological vesicles and fibers.

This imaging transformation and potential clinical translation of multiphoton microscopy is enabled by an emergent concept of laser-microscope alignment decoupling (Supplementary Fig. S1, Supplementary Discussion 2), which requires a synergic combination of deterministic single-mode coherent supercontinuum generation (Supplementary Discussion 3) and the arbitrary pulse shaping used typically in precision metrology or telecommunication applications[14] (Supplementary Discussion 4). Thus, an operator with no laser and optical alignment training could selectively display the spatial distribution of a specific endogenous substance on the computer screen, or instantly (and remotely if necessary) change the imaged substance to a different one by pushing preprogramed buttons that control the excitation/detection (Supplementary Table S1), with neither histological stains nor optical realignments.

In contrast to the vital signatures of various normal adipocytes, mast cells, and fibroblasts uniquely reflected by cell bodies (Fig. 2), tumor cells are shown in the 2PAF-SHG composite images to emerge from the metastatic environment of the cross-linked collagen network[15] inside a week-3 tumor, or are shown to be invading into the surrounding stroma in a week-8 tumor consisting of tumor-associated collagen signatures-2 (TACS-2) fibers that are aligned parallel to the tumor boundary[16,17] (Fig. 2). These normal and tumor-associated signatures are absent in the comparable H&E histology images of the same specimens due to the low or non-specific contrast of the extracellular matrix. The multiphoton images not only convey the unperturbed morphological information from various cells and the extracellular matrix, but also discriminate between tumor and normal cells by the 3PAF/2PAF signal ratio. The adipocytes (cell 3), mast or other stromal cells (cell 4, cell 5), and fibroblasts (cell 6) have a relatively small 3PAF signal, so they retain their yellow 2PAF color in the 2PAF–3PAF composite images. In contrast, the tumor cells (e.g., cell 7) in both tumors generate large co-localized 3PAF signal (presumably due to high levels of NADH during tumor-associated metabolism[18]), which gives these cells a blue appearance. An invasion front at the tumor-stroma boundary can be identified in the week-8 tumor by the invading tumor cells and the numerous "disorganized" 3PAF-lightened vesicles seemly derived from the tumor cells. The presence of significant co-localized 3PAF signal can then discriminate the tumor cells in the week-6 tumor (Fig. 1, cell cluster 1) from the normal cells in the week-3 tumor margin specimen (Fig. 1, cell cluster 2), despite their similar irregular morphology. Small but appreciable R2850 (lipid) signals can also be found to co-localize with the 2PAF-visible tumor cells (Fig. 1, left, R2850 image) but not the normal cells in Fig. 2, suggesting *de novo* lipogenesis associated with the tumor cells[19,20]. Experienced pathologists can discriminate tumor and non-tumor cells/specimens from the histology images alone (Figs. 1, 2), but cannot necessarily deduce any metabolic information.

We were also able to demonstrate a potential quantitative breast cancer biomarker in this rat model. The tumors can be objectively discriminated against non-tumor specimens by the emergence of an R3050 spectral peak in the hyperspectral image-integrated CARS spectra (Figs. 1, 2). This R3050 signal is not from the carcinogen (N-nitroso-N-methylurea) injected into the rats because spectral focusing of CARS on a saturated water solution of the carcinogen (1.4% by weight) did not yield any signal at R3050. Because regions within mammary specimens can be largely classified into stromal regions (Supplementary Fig. S2) and adipose regions (Supplementary Fig. S3) that account for 25% and 75% of the total area from control specimens, respectively, it is more representative to examine comparable tumor and non-tumor specimens that contain both regions (Supplementary Fig. S4). The R3050 spectral peak readily differentiates tumor and non-tumor specimens, even though their morphological differences are subtle and tumor cells may not be present. By comparing Supplementary Fig. S4 with the multimodal images and the integrated CARS spectra from the stromal regions (Supplementary Fig. S2) and adipose regions (Supplementary Fig. S3), we can conclude that this peak emerges only from the stromal regions. In the videos consisting of hyperspectral CARS images, the cancer biomarker manifests itself as a “flash” at R3050 in the stromal regions but not in the adipose regions (Supplementary Videos 1–3). This potential biomarker is robust against the presence of various marked structures that could have complicated qualitative morphological-based interpretation (Figs. 1, 2, Supplementary Fig. S2). Because this region-dependent hyperspectral cancer biomarker cannot be appreciated by either imaging or spectroscopy alone, the advantage of hyperspectral CARS imaging for the detection and spatial mapping of this biomarker is self-evident.

In all tumor specimens (Figs. 1, 2, Supplementary Figs. S2, S4), considerable R3050 signal co-localized with the 2PAF-visible tumor cells, which was more pronounced than the R2850 signal that reflects *de novo* lipogenesis, and thus gives these cells a gray appearance in the composite 2PAF-R3050 images (Figs. 1, 2). Non-tumor cells have little contrast in both the R3050 and R2850 images (Figs. 1, 2, Supplementary Figs. S2, S4). Also, mammary tumors seem to generate the R3050-peak phenotype, which was also widely found in normal spleen, liver, lung, skin, and muscle from control rats. The mammary tumor cells in Fig. 2 resemble the biosynthesis-active normal cells in the spleen and liver which exhibit co-localized cell contrast from 2PAF, R3050, and R2850 (Supplementary Fig. S5). This evidence suggests that the metabolic biomolecules associated with the on-and-off R3050 breast cancer biomarker are produced by the tumor cells with a metabolism switched to mainly biosynthesis (Warburg effect)[21], and become transported away from tumors to tumor margins (Fig. 1, right; Fig. 2, middle). These findings suggest that the histologically normal specimens exhibit evidence of this R3050 biomarker and its association with early changes in carcinogenesis. These results suggest that the R3050 cancer biomarker could potentially enable cancer diagnosis at a very early stage (week 1), when no tumor is palpable and gross examination is indeterminate (Supplementary Table S3). The observation of a similar cancer biomarker in humans would potentially allow for early and quantitative diagnosis from small biopsy specimens that may or may not sample the tumors directly.

As a second example, multiphoton images of a week-8 tumor in Fig. 2 demonstrate the migration of 2PAF/R3050-visible tumor cells or cell debris that collectively represent tumor

cell migration/invasion[22] (CTCI, Fig. 3, left panel; Supplementary Fig. S6). The "disorganized" 3PAF-visible vesicles in Fig. 2 become part of another extension of organizing vesicles infiltrating from the tumor into the surrounding stroma (An; Fig. 3, left panel; Supplementary Figs. S6–S8). In another specimen, there is image-based evidence that the vascularized stroma in the cancerous tissue is degrading adipose tissue, supporting the previous literature that these vesicles can be linked to angiogenesis[23,24], a known hallmark of cancer[25]. The relatively well developed blood vessels (BV) have 2PAF-visible internal epithelial cells but sparse 3PAF-visible vesicles, while the angiogenic vessels (An) have no such epithelial cells but show an abundance of such vesicles (Fig. 3, right). Similar to the adipocytes, mast cells, and fibroblasts in Fig. 2, these vasculature-revealing epithelial cells have minimum (or uniform) contrast in 3PAF (or CARS) (Supplementary Figs. S8, S9), and are therefore suggestive of non-malignant normal cells. Different from angiogenesis via the classic sprouting mechanism[26], the observed angiogenesis is accompanied by reorganized collagen networks (Supplementary Fig. S8), including a third extension of TACS-3 collagen fibers perpendicular to the TACS-2 collagen fibers[16,17] to assist the collective tumor cell invasion (Fig. 3, left) and angiogenesis-accommodating collagen reorganization. A TACS-1 aggregate of fibrosis can also be identified[16,17] (Fig. 3, right panel). Numerous elastin fibers form a fourth extension in concert with the above three (LA, Supplementary Fig. S6), and may be associated with the formation of the elastin basket in Fig. 1, to ultimately evolve into the leaky elastin-containing basement membrane known to enclose lymphatic vessels (LV, Fig. 2; Supplementary Video 4), i.e., to enable tumor lymphangiogenesis[27] (LA, Supplementary Fig. S7).

These linked events of collective tumor cell invasion, tumor associated collagen reorganization, and (lymph-)angiogenesis reflect the vital signatures of local tumor invasion present in fresh tissue being imaged with this multimodal multiphoton microscope. While experienced pathologists can identify the tumor cells and high-density distorted blood vessels suggestive of angiogenesis in the comparable histology images (Fig. 3), the additional information and findings from the fresh tissue microenvironment of local tumor invasion are often missing due to the weak signal, strong interfering background, and histology-induced structural changes (Figs. 1, 2). It should be noted that the four parallel extensions of tumor cells or cell debris, angiogenic vesicles, reorganized collagen fibers, and lymphangiogenic elastin fibers are largely obscured by the strong interfering background in the composite multimodal image (Fig. 3, left panel), but emerge when the imaging contrasts are unmixed (Supplementary Fig. S6). It is then conceivable that the absence of these optical signatures in the comparable histology images originates more from contrast interference than a lack of signal. Thus, the arbitrary mixing and unmixing of a large number (>5) of different contrasts (Figs. 1–3, Supplementary Figs. S2–S9) makes our stain-free histopathology advantageous over standard histopathology.

To conclude, the use of stain-free histopathology offers several significant advantages. Rapid, stain-free imaging of fresh thin or thick tissue specimens is possible with short turnaround times for disease diagnosis that could even supersede surgical frozen-section analysis, in contrast to more conventional histological tissue fixation, processing, and staining that often requires lengthy preparation time. Image generation can result from a microscope platform without the need for extensive wet laboratory facilities and a team of

histotechnologists. Without the need for tissue fixation and processing that include the use of formalin[28], xylene[29], or other toxic chemicals, there are possible environmental and healthy workplace benefits. While our stain-free histopathology will not completely replace standard H&E histopathology as the gold standard, the hematoxylin, eosin, other histochemical stains, and antibody or nucleic acid immunohistochemistry probes may be replaced by the programmable light that generates tailored chemical contrasts, not only from the demonstrated five modalities but also from transient[5] or nonlinear absorption[30], stimulated emission[31], wave mixing[32], etc. Because the light served as a programmable variable within a broad excitation/detection map that was tailored to probe specific endogenous substances (Supplementary Table S2), it can be easily reprogrammed to target different substances of interest, as well as biological samples with varying chemical composition and interfering backgrounds (Supplementary Table S1). The “virtual” histochemistry achieved by manipulating light is advantageous over the current immunohistochemistry because a large number of molecular markers can be imaged in a single tissue section to maximize the information at each pixel and capture crucial co-relationships between the markers (Figs. 1–3). Without the diverse molecular contrast from multiphoton interactions, this “virtual” histochemistry has been difficult to achieve in single-photon technologies based on confocal reflectance microscopy[33] (reflectance contrast), optical coherence tomography[34] (scattering contrast), and photoacoustic imaging[35] (absorption contrast). As representative data, this study demonstrated several known as well as new potential cancer biomarkers based on multimodal morphological and spectral signatures. Future investigations will utilize this data to further elucidate the complex mechanisms and biochemical processes in carcinogenesis as well as in other pathological processes in pre-clinical and clinical specimens.

Methods

1. Fiber supercontinuum generation

The 1041-nm 220-fs 80-MHz pulses from a Yb:KYW laser (femtoTRAIN IC model-Z, High Q Laser) were coupled by an aspheric lens (C330TME-C, Thorlabs) into a 21-cm custom-made photonic crystal fiber (NL-1050-NEG-PM-FUD, NKT Photonics) along the slow-axis of the fiber[36]. The linear birefringence of the fiber was estimated to be 4.2×10^{-4} by spectral interferometry, ensuring small (<0.5%) nonlinear depolarization along the fast axis of the 21-cm fiber. Thus, the variation of the spectrum due to the environmental changes was completely suppressed. The output (or input) coupling power was maintained at 480 (or 800) mW during all imaging sessions using a feedback control loop (Supplementary Fig. S1e). The output was collimated by an off-axis parabolic mirror and sent to the microscope. The parabolic mirror was aligned by optimizing the beam shape on a beam profiler at a long distance. The supercontinuum spectrum (780–1320 nm) was measured by an optical spectral analyzer daily to ensure reproducible operation. Throughout a one-year test period, this spectrum and the corresponding spectral phase have been reproducibly measured in daily operations, not only from one fiber segment but also from other 21-cm fiber segments. This demonstrates the reliable spectral phase stability of this source and ensures reproducible output power and polarization in routine daily operations. Without either the short-term quantum-noise instability or the long-term birefringence-induced instability[36], the supercontinuum enables high-quality multiphoton imaging of unstained biological samples.

2. Multimodality-empowered CARS microscope

A dichroic mirror (DMLP900, Thorlabs) was used to separate the supercontinuum into the CARS pump beam (780–880 nm) and the CARS Stokes beam (900–1320 nm) (Supplementary Fig. S1e). The Stokes beam was sent into a commercial pulse shaper (MIIPS Box640, Biophotonics Solutions) for not only CARS imaging, but also 2PAF, SHG, 3APF, and THG imaging. The two beams were then recombined by another dichroic mirror, steered into a commercial microscope (BX61WI, Olympus), and focused by a super-apochromat objective (UPLSAPO 60×W/IR N.A. = 1.20, Olympus). The super-apochromat microscope objective enabled diffraction-limited imaging independent of excitation wavelengths. Because many common micron-sized biological vesicles show up in all imaging modalities of rat spleen and liver specimens, co-localized multimodal imaging at the same imaging plane can be ensured (Supplementary Fig. S5). All the multiphoton signals were collected in the backward (epi-) direction by the same objective, spectrally filtered, detected by a common photomultiplier tube (H7421-40 Hamamatsu), and rigorously calibrated (see Supplementary Methods), allowing *ex vivo* diagnosis of thick tissues (Supplementary Fig. S9). A specimen (5×5 mm^2 area with ~1 mm thickness, typically) was placed on a microscope slide and sealed under a coverslip, while the imaging focal plane was placed ~10 μm below the sample surface. A relatively long pixel dwell time of 200 μs was used for all modalities, which is largely limited by the raster scanning speed (>100 μs pixel dwell time) of a mechanical stage to collect images. For the regular images (380 × 380 pixels with 0.5 μm pixel size) and the large-area images (1100 × 1100 pixels with 0.5 μm pixel size) presented in this study, it took 40 s and 5 min to collect each image, respectively.

All SHG, THG, CARS, and 2PAF images were plotted with the same dynamic range using the default setting of ImageJ (National Institutes of Health) from unprocessed raw data. For some 3PAF images that have low signals but recognizable morphological features, we tuned the dynamic range (brightness/contrast) to better show these features. Thus, our preprogrammed settings allowed direct comparison of all modalities within the dynamic range, except for 3PAF. Although 3PAF does not generate strong signals in some specimens, it does in other specimens and uniquely reveals a class of biological vesicles.

3. Pulse shaping-enabled “virtual” histochemistry

For 2PAF, SHG, 3APF, and THG imaging of endogenous molecules and structures, pulses of selected spectral ranges were compressed to the transform-limit by multiphoton intrapulse interference phase scan[37] using the technique of “local compression”[36]. The pulse shaper was utilized to spectrally select (and attenuate if necessary) the spectral bands (amplitude shaping) and to compensate the spectral phases measured at the objective focus (phase shaping)[38]. For CARS, an additional linear chirp of 4500 fs^2 after pulse compression was introduced into the Stokes beam by phase shaping for optimal performance of spectral focusing[39] within the detection vibrational band of 2700–3200 cm^{-1}. The spectrally focused vibrational frequency of CARS was controlled by an electric setting of the optical delay between the pump and Stokes pulses (Supplementary Fig. S1). The spectral resolution of the system was calculated to be 14 cm^{-1} based on the measured FWHM (19 cm^{-1}) of the 2913 cm^{-1} peak in the CARS spectrum of dimethyl sulfoxide (Supplementary Methods). This finite spectral resolution of CARS is mostly limited by the finite spectral resolution of the

pulse shaper (640 pixels to cover the 750–1350 nm bandwidth). Spectral-focusing CARS was then used to collect hyperspectral CARS images from the biological samples, each of which was obtained at one spectral-focusing delay that was varied among the images. CARS spectral intensity at each spectral-focusing delay (vibration frequency) was calculated by averaging the intensity of all pixels in the hyperspectral image corresponding to that vibration frequency. This simple treatment mimics wide-field Raman spectroscopy and was sufficient to distinguish tumor and normal specimens (Supplementary Fig. S4). Thus, pulse shaping enables optimization of optical signal generation across different modalities. The amplitude and compensation phase masks were then preprogrammed and applied in all imaging sessions. This can then demonstrate that exposing a biological sample to pulse-shaped excitations generates imaging contrast similar to staining the sample with various dyes or fluorescent antibodies. In other words, the endogenous biomolecules in various biological samples can be “artificially” (non-invasively) labeled by pulse-shaped excitations along certain detection spectral-channels, rather than being “physically” labeled by exogenous stains or other fluorescent agents.

4. Animal model and histology

Pre-clinical rat experiments were performed under a protocol approved by the Institutional Animal Care and Use Committee at the University of Illinois Urbana-Champaign. One group of female rats (F344, Harlan, 7-week old) was injected intraperitoneally with N-nitroso-N-methylurea (Sigma) at a concentration of 55 mg/kg to induce mammary tumors[10]. The left abdominal side received one injection and the right abdominal side received the second injection of equal dose one week later. This pre-clinical rat model is well established and known to induce mammary tumors reproducibly and deterministically through single point mutations. This model is suitable for investigating breast cancer development because the anatomical and pathological features, the hormone dependency, and the immunohistochemical responses of the lesions mimic human ductal carcinoma *in situ* (DCIS)[40–42]. Around 5 weeks after the second injection, tumors were palpable from the abdominal surface. An equal amount of saline was injected into the control rats to account for any possible effects from the physical injection. In a longitudinal study, 9 experimental and 9 control rats were euthanized 1–9 weeks after the second injection, and mammary tissue specimens and other organs were dissected and placed in saline before imaging (Supplementary Table S3).

During gross examination, excised mammary tissue was cut into small specimens (5×5 mm^2 area with ~2 mm thickness, typically) for multiphoton imaging. Tumor margin specimens were excised at sites 1–5 mm away from palpable tumors (orange-color granular formation). Standard FFPE-H&E histology was performed on some specimens, and histology images corresponding to the multiphoton images were obtained by searching similar areas under a microscope. Although our best effort was taken to find the exact sites of multiphoton imaging, we note that the histology images of the adipose-tumor boundary areas (Fig. 1, left), precancerous stroma-dominant areas (Fig. 1, right, Fig. 2, middle, Fig. 3, right), adipose-stroma boundary areas (Fig. 2, left), stroma-only areas (Fig. 2, second left), tumor-only areas (Fig. 2, second right), and tumor-stroma boundary areas (Fig. 2, right, Fig. 3, left) were typical for these representative sites.

Supplementary Material

Refer to Web version on PubMed Central for supplementary material.

Acknowledgments

This research was supported by grants from the National Institutes of Health (R01 CA166309 and R01 EB013723), Danish Council for Independent Research – Technology and Production Sciences (FTP project ALFIE), European Commission (EU Career Integration Grant 334324 LIGHTER), and by the Max Planck Society.

References

1. Titford M, Bowman B. What may the future hold for histotechnologists? Lab. Med. 2012; 43:e5–e10.
2. Buesa RJ. Histology: a unique area of the medical laboratory. Ann. Diagn. Pathol. 2007; 11:137–141. [PubMed: 17349575]
3. Denk W, Strickler JH, Webb WW. Two-photon laser scanning fluorescence microscopy. Science. 1990; 248:73–76. [PubMed: 2321027]
4. Zipfel WR, Williams RM, Christie R, Nikitin AY, Hyman BT, Webb WW. Live tissue intrinsic emission microscopy using multiphoton-excited native fluorescence and second harmonic generation. Proc. Natl. Acad. Sci. USA. 2003; 100:7075–7080. [PubMed: 12756303]
5. Matthews TE, Piletic IR, Selim MA, Simpson MJ, Warren WS. Pump-probe imaging differentiates melanoma from melanocytic nevi. Sci. Transl. Med. 2011; 3:71ra15.
6. Ji M, et al. Rapid, label-free detection of brain tumors with stimulated Raman scattering microscopy. Sci. Transl. Med. 2013; 5:201ra119.
7. Tao YK, Shen D, Sheikine Y, Ahsen OO, Wang HH, Schmolze DB, Johnson NB, Brooker JS, Cable AE, Connolly JL, Fujimoto JG. Assessment of breast pathologies using nonlinear microscopy. Proc. Natl. Acad. Sci. USA. 2014; 111:15304–15309. [PubMed: 25313045]
8. Lu F-K, et al. Label-free DNA imaging *in vivo* with stimulated Raman scattering microscopy. Proc. Natl. Acad. Sci. USA. 2015; 112:11624–11629. [PubMed: 26324899]
9. Zipfel WR, Williams RM, Webb WW. Nonlinear magic: multiphoton microscopy in the biosciences. Nat. Biotechnol. 2003; 21:1369–1377. [PubMed: 14595365]
10. Sukumar S, Notario V, Martin-Zanca D, Barbacid M. Induction of mammary carcinomas in rats by nitroso-methylurea involves malignant activation of H-ras-1 locus by single point mutations. Nature. 1983; 306:658–661. [PubMed: 6318112]
11. Chowdary PD, et al. Molecular histopathology by spectrally reconstructed nonlinear interferometric vibrational imaging. Cancer Res. 2010; 70:9562–9569. [PubMed: 21098699]
12. Chance B, Schoener B, Oshino R, Itshak F, Nakase Y. Oxidation-reduction ratio studies of mitochondria in freeze-trapped samples. NADH and flavoprotein fluorescence signals. J. Biol. Chem. 1979; 254:4764–4771. [PubMed: 220260]
13. Sutton, D. A textbook of radiology and imaging. New York, NY: Churchill Livingstone Inc; 1987.
14. Weiner AM. Femtosecond pulse shaping using spatial light modulators. Rev. Sci. Instrum. 2000; 71:1929–1960.
15. Levental KR, Yu H, Kass L, Lakins JN, Egeblad M, Erler JT, Fong SF, Csiszar K, Giaccia A, Weninger W, Yamauchi M, Gasser DL, Weaver VM. Matrix crosslinking forces tumor progression by enhancing integrin signaling. Cell. 2009; 139:891–906. [PubMed: 19931152]
16. Provenzano PP, Eliceiri KW, Campbell JM, Inman DR, White JG, Keely PJ. Collagen reorganization at the tumor-stromal interface facilitates local invasion. BMC Med. 2006; 4:38. [PubMed: 17190588]
17. Provenzano PP, et al. Collagen density promotes mammary tumor initiation and progression. BMC Med. 2008; 6:11. [PubMed: 18442412]
18. Skala MC, Riching KM, Gendron-Fitzpatrick A, Eickhoff J, Eliceiri KW, White JG, Ramanujam N. In vivo multiphoton microscopy of NADH and FAD redox states, fluorescence lifetimes, and

cellular morphology in precancerous epithelia. Proc. Natl. Acad. Sci. USA. 2007; 104:19494–19499. [PubMed: 18042710]

19. Menendez JA, Lupu R. Fatty acid synthase and the lipogenic phenotype in cancer pathogenesis. Nat. Rev. Cancer. 2007; 7:763–777. [PubMed: 17882277]
20. Le TT, Huff TB, Cheng JX. Coherent anti-Stokes Raman scattering imaging of lipids in cancer metastasis. BMC Cancer. 2009; 9:42. [PubMed: 19183472]
21. Vander Heiden MG, Cantley LC, Thompson CB. Understanding the Warburg effect: the metabolic requirements of cell proliferation. Science. 2009; 324:1029–1033. [PubMed: 19460998]
22. Friedl P, Gilmour D. Collective cell migration in morphogenesis, regeneration and cancer. Nat. Rev. Mol. Cell Biol. 2009; 10:445–457. [PubMed: 19546857]
23. Carmeliet P, Jain RK. Angiogenesis in cancer and other diseases. Nature. 2000; 407:249–257. [PubMed: 11001068]
24. Weis SM, Cheresh DA. Tumor angiogenesis: molecular pathways and therapeutic targets. Nat. Med. 2011; 17:1359–1370. [PubMed: 22064426]
25. Hanahan D, Weinberg RA. Hallmarks of cancer: the next generation. Cell. 2011; 144:646–674. [PubMed: 21376230]
26. Folkman J, Haudenschild C. Angiogenesis *in vitro*. Nature. 1980; 288:551–556. [PubMed: 6160403]
27. Stacker SA, Achen MG, Jussila L, Baldwin ME, Alitalo K. Lymphangiogenesis and cancer metastasis. Nat. Rev. Cancer. 2002; 2:573–583. [PubMed: 12154350]
28. Buesa RJ. Histology without formalin? Ann. Diagn. Pathol. 2008; 12:387–396. [PubMed: 18995201]
29. Buesa RJ. Histology without xylene. Ann. Diagn. Pathol. 2008; 13:246–256. [PubMed: 19608083]
30. Fu D, Ye T, Matthews TE, Chen BJ, Yurtserver G, Warren WS. High-resolution *in vivo* imaging of blood vessels without labeling. Opt. Lett. 2007; 32:2641–2643. [PubMed: 17873920]
31. Min W, Lu S, Chong S, Roy R, Holtom GR, Xie XS. Imaging chromophores with undetectable fluorescence by stimulated emission microscopy. Nature. 2009; 461:1105–1109. [PubMed: 19847261]
32. Mahou P, Zimmerley M, Loulier K, Matho KS, Labroille G, Morin X, Supatto W, Livet J, Débarre D, Beaurepaire E. Multicolor two-photon tissue imaging by wavelength mixing. Nat. Methods. 2012; 9:815–818. [PubMed: 22772730]
33. González S, Tannous Z. Real-time *in vivo* confocal reflectance microscopy of basal cell carcinoma. J. Am. Acad. Dermatol. 2002; 47:869–874. [PubMed: 12451371]
34. Huang D, et al. optical coherence tomography. Science. 1991; 254:1178–1181. [PubMed: 1957169]
35. Zhang HF, Maslov K, Stoica G, Wang LV. Functional photoacoustic microscopy for high-resolution and noninvasive in vivo imaging. Nat. Biotechnol. 2006; 24:848–851. [PubMed: 16823374]
36. Liu Y, Zhao Y, Lyngsø J, You S, Wilson WL, Tu H, Boppart SA. Suppressing short-term polarization noise and related spectral decoherence in all-normal dispersion fiber supercontinuum generation. J. Lightwave Technol. 2015; 33:1814–1820. [PubMed: 26166939]
37. Lozovoy VV, Pastirk I, Dantus M. Multiphoton intrapulse interference. IV. Ultrashort laser pulse spectral phase characterization and compensation. Opt. Lett. 2004; 29:775–777. [PubMed: 15072388]
38. Liu Y, Tu H, Benalcazar WA, Chaney EJ, Boppart SA. Multimodal nonlinear imaging by pulse shaping of a fiber supercontinuum from 900 to 1160 nm. IEEE J. Sel. Top. Quantum Electron. 2012; 18:1209–1214.
39. Pegoraro AF, Ridsdale A, Moffatt DJ, Jia Y, Pezacki JP, Stolow A. Optimally chirped multimodal CARS microscopy based on a single Ti:sapphire oscillator. Opt. Express. 2009; 17:2984–2996. [PubMed: 19219203]
40. Arafah BM, Finegan HM, Roe J, Manni A, Pearson OH. Hormone dependency in N-nitrosomethylurea-induced rat mammary tumors. Endocrinology. 1982; 111:584–588. [PubMed: 7094887]

41. Crist KA, Chaudhuri B, Shivaram S, Chaudhuri PK. Ductal carcinoma *in situ* in rat mammary gland. J. Surg. Res. 1992; 52:205–208. [PubMed: 1311399]

42. Singh M, McGinley JN, Thompson HJ. A comparison of the histopathology of premalignant and malignant mammary gland lesions induced in sexually immature rats with those occurring in the human. Lab. Invest. 2000; 80:221–231. [PubMed: 10701691]

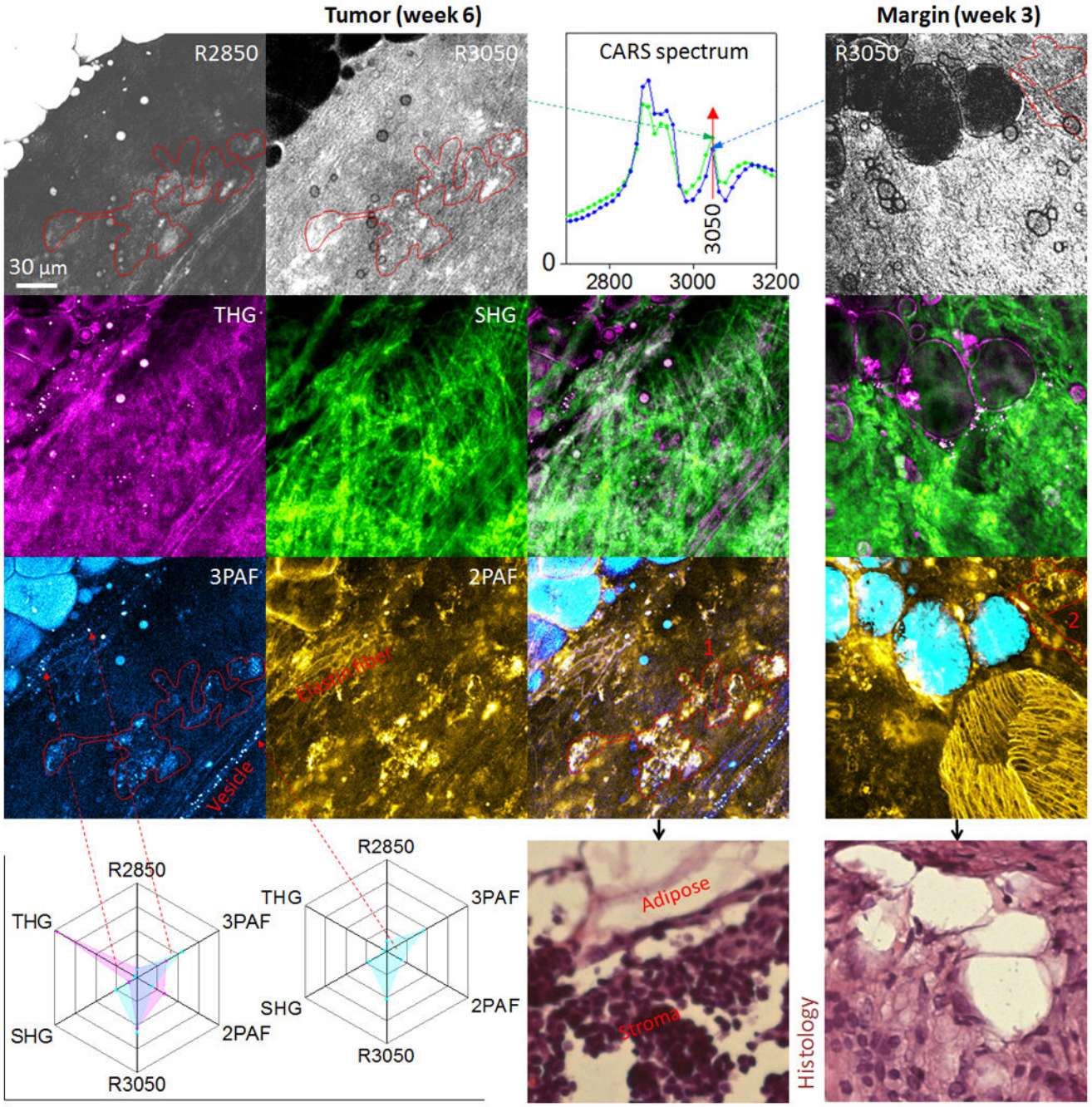

Figure 1. Mesoscopic organization of biological microstructures revealed in co-localized multiphoton images of two rat mammary specimens and absent from corresponding FFPE-H&E histology images

Area-integrated CARS spectra over 34 hyperspectral images confirm the presence of a significant R3050 peak (see text for details) as a potential cancer biomarker. (Left): Different histochemical components of a tumor are selectively revealed by different single-modality images. Cell cluster 1 (red outline) is identifiable in a 2PAF image, and also in 3PAF, R3050, and R2850 images, reflecting tumor-associated metabolism (see text for details). The hexagonal radar multiphoton profile (9-pixel average) of a specific type of isolated vesicle

approximates that of vesicles aligned in a tubular formation, suggesting that these vesicles are distributed more diffusely before organizing into a tube (indicative of angiogenesis, see text for details). (Right): Cell cluster 2 (red outline) in a specimen with histologically unidentified cancer from a carcinogen-injected rat is identifiable in a 2PAF image, but not in R3050 and other images, reflecting normal cellular metabolism. Elastin fibers widely observed in connective tissue are shown to be organized into a “basket”, which can be linked to lymphangiogenesis (see text for details). Multiphoton image size: 380 × 380 pixels with 0.5 μm pixel size.

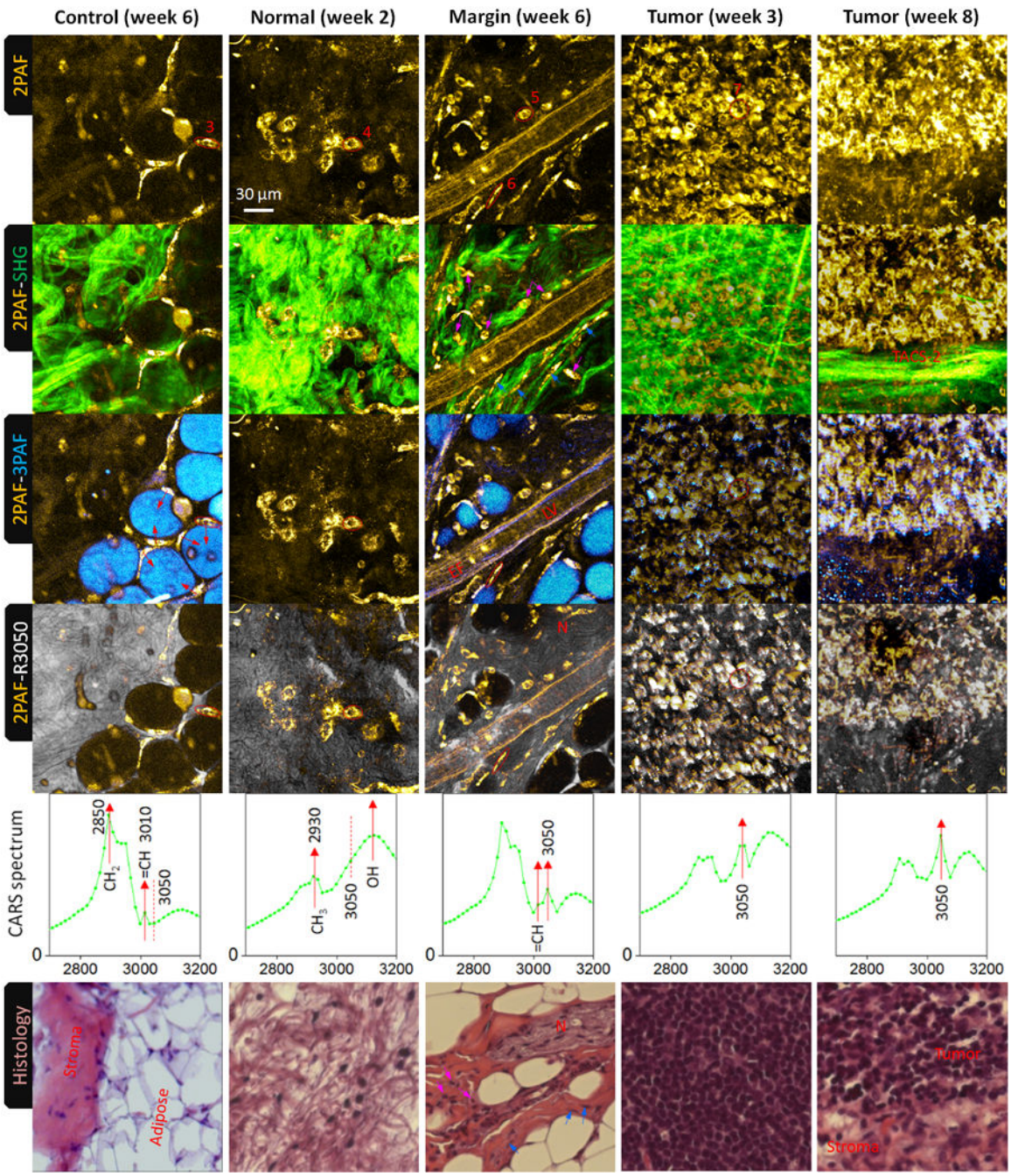

Figure 2. Optical signatures in co-localized multiphoton images of five mammary specimens that are absent from corresponding FFPE-H&E histology images

Area-integrated CARS spectra over 30 hyperspectral images reveal common molecular vibrations of CH_2 (2850 cm^{-1}), CH_3 (2930 cm^{-1}), =CH (3015 cm^{-1}), and OH stretches (3000–3200 cm^{-1}), and exhibit a cancer biomarker at R3050, whereas cross-modality visibilities of 2PAF-enhanced cells (encircled in red and labeled #3–7) represent distinct cellular metabolic states. (Bottom row): histology delineates characteristic adipose and stromal regions of control mammary tissue, and reveals cell nuclei located in interstitial spaces among lipid vacuoles of adipocytes with no correspondence between cell nuclei and

lipids. In multiphoton images, however, 2PAF-visible cell bodies in the background of 3PAF-visible lipids point to the unique relationship between cell bodies and lipids (red arrows) that form complete adipocytes. (Bottom row, second left): histology of a stroma-only region from a normal appearing mammary specimen (no palpable tumor) from a carcinogen-injected rat displays only some cell nuclei scattered in a distorted collagen fiber network, whereas multiphoton images show how several cells orient themselves in the voids of the collagen fiber network. (Bottom row, middle): histology identifies fibroblasts (blue arrows) from mast cells (magenta arrows) at a tumor margin approximately 1 mm away from a palpable week 6 tumor. In multiphoton images, however, spindle-shaped collagen-producing fibroblasts are aligned with SHG-visible collagen fibers and can be easily differentiated from mast cells near a lymphatic vessel (LV) with flowing lymph (Supplementary Video 4) and a leaky 2PAF-visible basement membrane containing elastin fibers. (Second right): multiphoton images of the inside of a non-palpable tumor reveals cross-linked collagen network that assists tumor invasion. (Right): multiphoton images at a tumor-stroma boundary exhibit vital signatures of local tumor invasion across TACS-2 collagen. Abbreviations: EF – elastin fibers; N– nerve; LV – lymphatic vessel; TACS – tumor-associated collagen structure. Multiphoton image size: 380 × 380 pixels with 0.5 μm pixel size.

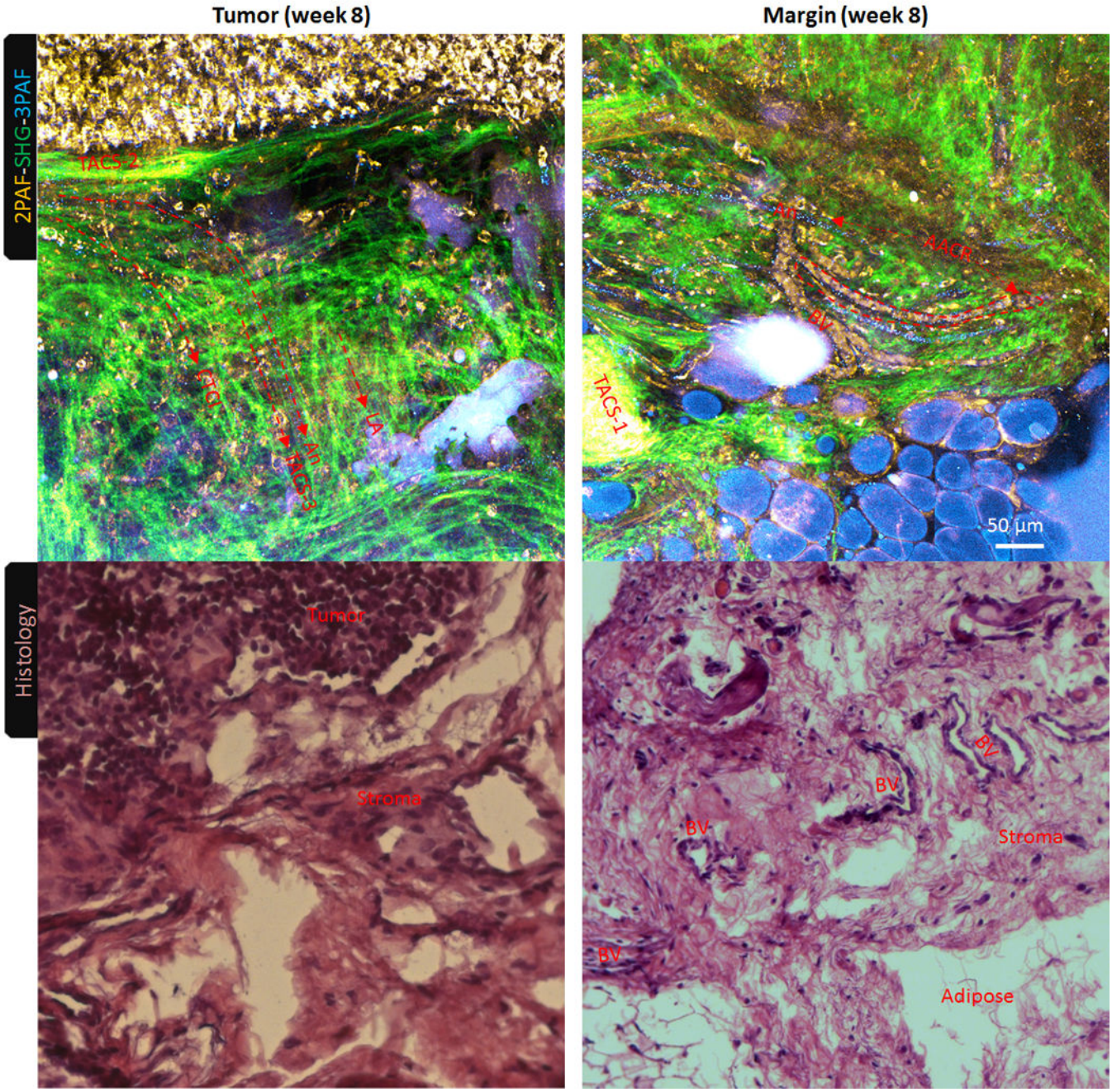

Figure 3. Optical signatures of local tumor invasion in large-area tri-modal multiphoton images of two rat mammary specimens that are absent from corresponding FFPE-H&E histology images

The margin specimen was excised approximately 1 mm away from the tumor. Directed local tumor invasion (downward in image) at the tumor-stroma boundary (left) and degradation of adipose tissue by vascularized stroma at the tumor margin (right) are recognized in the multiphoton images, but only the former can be revealed in standard H&E histology. In the latter case, the 3PAF-visible angiogenesis (An) is absent and naturally branched 2PAF-visible blood vessels (BV) become distorted and fragmented in the histology image so that

the tumor-associated angiogenesis is hardly detectable. In both cases, several vital optical signatures (arrows) of local tumor invasion are largely obscured by a strong interfering background in the tri-modal multiphoton images, just like in histology, but emerge when the contrasts of individual multiphoton modalities are unmixed (see Supplementary Figs. S6–S9 and text for details). Abbreviations: AACR – angiogenesis-accommodating collagen reorganization; An – angiogenesis; BV – blood vessel; CTCI – collective tumor cell invasion; LA – lymphangiogenesis; TACS – tumor-associated collagen structure. Multiphoton image size: 1100 × 1100 pixels with 0.5 μm pixel size.